PNAS

Supporting Information for

Perturbative diffraction methods resolve a conformational switch that facilitates a two-step enzymatic mechanism

Jack B. Greisman, Kevin M. Dalton, Dennis E. Brookner, Margaret A. Klureza, Candice J. Sheehan, In-Sik Kim, Robert W. Henning, Silvia Russi, and Doeke R. Hekstra*

***E-mail: doeke_hekstra@harvard.edu**

This PDF file includes:

Supporting text
Figs. S1 to S4
Tables S1 to S11
SI References

Supporting Information Text

Materials and Methods

A. Protein Purification and Crystallization. We expressed, purified, and crystallized *ec*DHFR as described previously (1), with one modification. In order to purify *ec*DHFR for the complex with 10-methylfolate, we modified the methotrexate-affinity chromatography to include a wash with 200 mM potassium phosphate buffer (pH 6.0) with 1 M potassium chloride, 1 mM ethylenediaminetetraacetic acid (EDTA), and 1 mM dithiothreitol (DTT) and elution the protein using a linear gradient with 50 mM potassium borate buffer (pH 10.15) and 2 M potassium chloride. The high pH, high salt elution was necessary to avoid contamination of the purified protein with bound folate. We used crystals of the model of the Michaelis complex, *ec*DHFR:FOL:NADP$^+$, for the multi-temperature X-ray diffraction experiments and the electric-field-stimulated X-ray diffraction (EF-X) experiments. We co-crystallized the 10-methylfolate (No. 16.211, Schircks Laboratories) complex using the same conditions as the *ec*DHFR:FOL:NADP$^+$ complex (1).

B. Monochromatic Data Collection. We collected the 10-methylfolate complex and multi-temperature datasets presented in this work at the Stanford Synchrotron Radiation Lightsource (SSRL) beamline 12-1 at the SLAC National Accelerator Laboratory. We collected the data during three beamtime allocations on July 20, 2021; November 10, 2021; and May 7, 2022. We looped all crystals at Harvard University using the MicroRT system (MiTeGen) for room-temperature data collection, and shipped the looped crystals to SSRL 12-1 using the SSRL *in situ* Crystallization Plate (M-CP-111-095, Crystal Positioning Systems) and a thermal shipping container to maintain the samples at 277 K. The specialized plate was used for compatibility with the robotic sample handling at SSRL 12-1, which supported remote data collection at regulated temperatures and high humidity (2); see also https://www-ssrl.slac.stanford.edu/smb-mc/content/users/manuals/remote-access-at-elevated-temperatures-and-controlled-humidity. The SSRL 12-1 beamline uses the 800 Series Cryostream Cooler (Oxford Cryosystems) for temperature regulation, which maintains the sample position temperature to within 0.1 K.

For all monochromatic diffraction experiments we used helical data acquisition, translating along the long-axis of the rod-shaped crystals to best distribute the radiation dose among the crystal volume. Unless otherwise noted, the beam size was set to 50×50 µm^2, 0.2% transmission, and at 15.00 keV. On average, the crystals were $75 \times 75 \times 500$ µm, and we collected 1440 images with a 1° oscillation angle and a 0.2 s exposure time. SSRL BL12-1 is equipped with an Eiger 16M detector (Dectris) with a pixel size of 75 µm^2. We began each crystal at 295 K, and adjusted the environmental temperature to the desired set point at a ramp rate of approximately 2 °/min. Based on the crystal properties, beam parameters, and helical acquisition, we estimated the average diffraction weighted dose to be $\sim$0.2 MGy per dataset using RADDOSE-3D (3, 4). For the single-crystal, multi-temperature experiments, this corresponds to a maximum estimated dose of $\sim$1.0 MGy per-crystal.

10-methylfolate Complex. We collected the diffraction data for the 10-methylfolate complex with a beam size of 50×7 µm^2 at 13.00 keV, a detector distance of 160 mm, and at 285 K.

Multi-temperature Diffraction Experiments. To investigate the conformational changes in DHFR across a range of physiological temperatures, we collected 4 datasets at 270 K, 5 datasets at 280 K, 5 datasets at 290 K, 1 dataset at 295 K, 5 datasets at 300 K, and 3 datasets at 310 K. For these experiments, we collected a single dataset at the desired temperature from each crystal, using an incident beam energy of 15.00 keV and a detector distance of 160 mm. To facilitate the use of isomorphous difference maps to identify structural differences, we also collected multiple datasets at different temperatures from the same crystal. For one crystal, we collected successive datasets at 295 K, 280 K, 295 K, 310 K, and 295 K, and for another crystal we collected the reversed series at 295 K, 310 K, 295 K, 280 K, and 295 K. The repeated measurements at 295 K allowed us to assess hysteresis and to rule out radiation damage, as indicated by the relatively flat isomorphous difference maps from successive datasets.

Data Reduction, Scaling, and Structure Refinement. We used *DIALS* to find and index strong spots, refine the experimental geometry, and integrate each dataset at each temperature (5). Each dataset was processed independently, using default parameters in *DIALS*. During indexing we provided the space group, $P2_12_12_1$, and used local index assignment (`index.assignment.method=local`). This improved the indexing rate by reducing the sensitivity to small crystal motions during the course of helical data acquisition. Following geometry refinement, the residuals for spot prediction were approximately 0.2-0.3 px (RMSD).

The relative scale of each dataset is an important consideration when using difference maps to visualize conformational changes between conditions. We used `dials.scale` with a common reference dataset, collected during the same day at 295 K, to ensure a consistent relative scale across all of our data (6). In addition to scaling and merging each dataset individually, we scaled and merged data collected at the same temperature from multiple crystals to refine single, representative structures for each temperature. High-resolution cutoffs were always chosen such that the half-dataset correlation coefficient of the highest resolution bin was greater than 0.3 (7). In all cases, the high resolution cutoff was < 1.35 Å, and the majority of the crystals diffracted to between 1.05 and 1.15 Å.

Due to the large number of diffraction datasets involved in this study, we chose an automated structure refinement protocol. We used `phenix.refine` (8) to refine occupancies, anisotropic B factors for all non-hydrogen atoms, and reciprocal space XYZ refinement to improve the atomic coordinates. Ligand geometry restraints for NADP$^+$, folate, 10-methylfolate, and oxidized cysteine (cysteine sulfinic acid) were generated using `phenix.elbow` using default parameters. Due to the high degree of similarity between each dataset, we initialized each refinement run by isomorphous replacement, and we found ten macrocycles to be sufficient to converge the refinement R factors. Importantly, to ensure that R-factors were comparable between runs, we used a common R-free set composed of 5% of the unique reflections.

Analysis of Multi-crystal, Multi-temperature Experiment. To identify temperature-dependent structural changes from refinement, we analyzed changes in pairwise distances between refined C_α coordinates. For residues refined with alternate conformations, only the highest occupancy conformer was included in the analysis. We used the *SciPy* library (9) to compute the pairwise distances between coordinates. These distances were treated as features and computed for the consensus structures at each temperature, yielding a $N \times d$ matrix with N datasets and d features. To prioritize analysis of how the structures differed, we subtracted the mean of each pairwise distance from the corresponding rows of the matrix. We then used singular value decomposition in *NumPy* (10) to analyze the primary temperature-dependent mode among the datasets.

Isomorphous Difference Maps. This work presents weighted isomorphous difference maps across temperatures and between different ligand-bound complexes. These maps used difference structure factor amplitudes, $|\Delta F_H|$, given by

$$|\Delta F_H| = w_H \left(|F_{H,cond2}| - |F_{H,cond1}|\right) \qquad [1]$$

where $|F_{H,cond1}|$ and $|F_{H,cond2}|$ are the merged structure factor amplitudes for the first condition and second condition, respectively, and w_H are weights defined as follows (11):

$$w_H = \left(1 + \frac{\sigma^2_{\Delta F}}{\overline{\sigma^2_{\Delta F}}}\right)^{-1} \qquad [2]$$

To emphasize the high-resolution features of the difference maps, we excluded low resolution reflections (> 5.0 Å) from the maps following Schmidt *et al.* (12). To facilitate the reproducibility of these difference maps, we added a command-line script, *rs.diffmap*, to the *rs-booster* command-line interface of *reciprocalspaceship* (13). The maps produced in this research used the arguments: *-a 0.0*, to achieve the weight function above, and *–dmax 5.0*, to exclude low-resolution reflections.

Validation of Temperature-resolved Difference Maps. To rule our artifacts, we used interleaved datasets collected at 295 K to assess radiation damage and reversibility of temperature-dependent effects, and further used two crystals with reversed temperature sequences to rule out hysteresis (Fig. S1A). Indeed, the refined hinge distance was reversible and did not depend on the order of temperature changes, suggesting our temperature ramps allowed sufficient equilibration time (Fig. S1B). Isomorphous difference maps between different temperatures obtained from single crystals exhibited notably stronger difference density than maps computed between datasets collected at the same temperature (Fig. S1C and S1D), confirming that the temperature difference explains the observed effects. Equivalent temperature-resolved differences from two independent crystals were strongly correlated (Fig. S1E), demonstrating reproducibility.

C. Electric-field-stimulated X-ray (EF-X) Diffraction.

Experimental Apparatus and Data Collection. We conducted the EF-X experiments at BioCARS (Advanced Photon Source, Argonne National Laboratory) using an experimental apparatus based on work by Hekstra *et al.* (14), with several important modifications that reduced sample attrition. These improvements are summarized below, and will be described in detail in an upcoming publication. The electrodes in the original experiment used wires threaded within glass capillaries, which could become retracted during sample handling, damage the crystal, and result in an osmotic mismatch with the crystal. To resolve this problem, we constructed solid state electrodes with flush surfaces for crystal contact. We produced bottom electrodes by threading tungsten wire (41 µm diameter) into glass microcapillaries (0.018 in O.D., 0.0035 in I.D., 16 mm length; Drummond) and fusing the glass around the tungsten with a Bunsen burner. We trimmed the protruding wires at the melted ends of the capillaries, and polished the electrode tips using a series of fine grit sandpapers to make a flat, flush surface with an exposed conductive patch. These bottom electrodes were placed in 3D-printed inserts compatible with reusable goniobases (Mitegen, SKU: GB-B3-R-20).

In addition, the original apparatus used a top electrode with an integrated pneumatic pump to establish liquid contact with the crystal (14). This design required brief exposure of the crystal to the air as liquid contact was being established, risking crystal dehydration. Here, we mounted crystals on the bottom electrodes and used Sylgard 184 (Dow-Corning) to insulate their electrical contact as previously described (14); however, we also pipetted a band of well solution in a polyester (PET) sleeve (MiTeGen) with approximately 10 µL of the crystal's mother liquor (Fig. S2A). Prior to the experiment, we cut the sleeve above the liquid band and brought the top electrode through the mother liquor, maintaining a high humidity environment for the crystal for the duration of the experiment. Using an adjustable kapton sleeve fitted to the top electrode, we created a small droplet of mother liquor at the end of the top electrode that we used to establish liquid contact with the crystal.

Finally, we used a custom, dual-polarity pulse generator from FID GmbH (Burbach, Germany) to generate high-voltage pulses for EF-X experiments. This pulse generator is available at the BioCARS 14-ID-B beamline. For the experiment presented here, we used the data collection strategy described in Hekstra *et al.* (14) with the following modifications. At each crystal orientation, we collected an X-ray diffraction image without electric field ('Off'), a diffraction image 200 ns after the application of a 250 ns high-voltage pulse at +3.5 kV, and a third image 200 ns after the application of a 250 ns pulse at -3.5 kV. We included a one second delay between images to permit crystal relaxation. After the three images at each crystal orientation, we rotated the crystal and repeated the collection sequence to fully sample reciprocal space (Fig. 4C). We collected the data reported here from 0° to 180° in 2° steps, from 181° to 361° in 2° steps, and from 361.5° to 541.5° in 1° steps. This progression achieves rapid coverage of reciprocal space to ensure high completeness while evenly distributing the radiation dose during acquisition. The Laue X-ray pulses had a 100 ps duration and a spectrum from 1.02 − 1.18 Å (approximately 5% energy bandwidth), peaked at 1.04 Å.

Data Reduction and Analysis of Reciprocal Space Signal. We indexed, refined the experimental geometry, and integrated the diffraction data using Precognition (Renz Research, Inc.). To scale and merge the time-resolved datasets while enforcing a common relative scale, we used `careless`, which employs approximate Bayesian inference to learn a generative model for the observed intensities and posterior estimates of the desired structure factor amplitudes (15). We provided the image numbers, inferred wavelength of each observation, observed Miller indices, the interplanar spacing, and the observed spot centroid on the detector to `careless` as metadata. We chose a Student's t-distribution with $\nu = 32$ for the likelihood function based on the evaluation of values of ν in the merging of the 'Off' dataset in $P2_12_12_1$. For processing with `careless`, we provided the 'Off' data in both $P2_12_12_1$ and the electric-field-reduced-symmetry spacegroup, $P2_1$ and provided the +3.5 kV and -3.5 kV datasets in $P2_1$. Data collection and processing statistics for this EF-X dataset are presented in Table S10.

To evaluate the presence of electric-field-dependent structural changes in the time-resolved dataset, we took advantage of the crystallographic symmetry operations that were broken by the electric field. In particular, the two-fold screw axes along the a- and c-axes are broken, whereas the two-fold screw axis along the b-axis is preserved due to the alignment of the crystal relative to the applied electric field. We can compare the merged structure factor amplitudes between regions of reciprocal space that were formerly related by crystallographic symmetry in order to identify electric-field-dependent signal. In the 'Off' data, processed in $P2_1$, this symmetry should be intact, resulting in a half-dataset correlation coefficient of zero for the differences between the regions of reciprocal space. On the other hand, these differences should be measurable and reproducible for the datasets collected in the presence of an applied electric field, yielding a positive correlation coefficient. This metric, CC_{sym}, is analogous to the half-dataset anomalous correlation coefficients (CC_{anom}) used to evaluate anomalous signal, but measures breaking of a spacegroup symmetry operation, here $(x + \frac{1}{2}, \frac{1}{2} - y, \overline{z})$, rather than Friedel's law $(\overline{x}, \overline{y}, \overline{z})$. We implemented CC_{sym} using `reciprocalspaceship` (13) and the result is shown in Fig. S2B.

Extrapolated Structure Factor Refinement. To refine the excited state structure induced by the application of an electric field, we used extrapolated structure factor (ESF) refinement (14, 16). To maximize the signal for our analysis, we refined the difference between the +3.5 kV and the -3.5 kV timepoints ('On' state) as follows:

$$F_H^{ESF} = |n(F_H^{+3.5kV} - F_H^{-3.5kV}) + F_H^{Off}| \qquad [3]$$

where n is the extrapolation factor, F_H^{Off} are the 'Off' state's structure factor amplitudes, merged in $P2_1$, and $F_H^{+3.5kV}$ and $F_H^{-3.5kV}$ are the structure factor amplitudes for the +3.5 kV and -3.5 kV HV pulses, respectively. We scaled the $F_H^{+3.5kV}$ and $F_H^{-3.5kV}$ datasets relative to the F_H^{Off} using *SCALEIT* (17), prior to computing ESFs. We computed σ_H^{ESF} by propagating uncertainties in quadrature, and we took the absolute value of the extrapolated structure factors to avoid negative values during refinement. This assumes that the corresponding phase for the structure factor is flipped by 180°. For refinement of the excited states, we constructed an appropriate reduced-symmetry space group by removing any crystallographic symmetry axes not collinear with the electric-field (14). In our experiment, the crystal was mounted with the b-crystallographic axis offset by $24.1 \pm 0.5°$ (mean ± std; $N = 1089$ images) relative to the electric field vector, such that the field component along the b axis equals $cos(24.1°) \approx 91\%$ of the full field. In this approximation we can treat the unit cell as consisting of two copies of a redefined asymmetric unit in the $P1\ 2_1\ 1$ spacegroup. To determine the extrapolation factor, we scanned values between 0 and 15 and ran automated structure refinement beginning from a model refined to the 'Off' data in $P2_12_12_1$. We found that the two copies of DHFR in the asymmetric unit refined to different hinge distances as a function of increasing n (Fig. S2C). The difference in hinge distance increased linearly until $n = 8$ and then plateaued at a difference of approximately 0.2 Å. As in Hekstra *et al.*, we chose the extrapolation factor to compromise between map quality (best at lower n) and the appearance of map features that correspond to strong peaks in the difference maps (stronger features at higher n) (14). We chose an extrapolation factor of $n = 8$ for further ESF refinement because it was the lowest value (best map quality) at which the full difference in hinge distance between the two copies was realized. We used `phenix.refine` for ESF refinement (8) using isotropic B factors, occupancies, and reciprocal space-based refinement of coordinates. The refinement statistics for the 'Off' state from Laue diffraction and the ESF refinement of the 'On' state are presented in Table S11. Although ESF refinement yields higher refinement R-factors than expected for a model at 1.70 Å resolution, the magnitude of these R-factors is not a reliable measure of model quality because of the increased influence of measurement error in the extrapolated structure factors. However, since the measurement error is unchanged during refinement, relative changes in R_{work} and R_{free} are still useful to guide structure refinement (14). To validate that the observed structural differences between the protein molecules of the excited-state ASU could not be explained by modeling bias, we generated simulated annealing (SA; `annealing_type=cartesian`) composite omit maps using default settings in PHENIX (18, 19). The SA composite omit maps are presented in Figure S3.

D. Molecular Dynamics (MD) Simulations. To directly validate mechanistic models of the dynamics observed by X-ray diffraction, we used MD simulations of DHFR in the crystal lattice and in solvated systems. These simulations were run using *OpenMM* (20), using a custom library written to support these types of simulations (https://github.com/JBGreisman/mdtools). We ran all simulations, unless otherwise noted, in an NPT ensemble at 298 K with a 2 fs timestep, and used the Amber14SB forcefield for the protein and ions (21) and the TIP3P model for water (22). We parameterized Folate and dihydrofolate (with and without protonation on the N5 nitrogen) using the general amber forcefield (GAFF) (23) and obtained amber-compatible NADP$^+$ and NADPH parameters from the Bryce group's database of cofactors (http://amber.manchester.ac.uk) (24, 25). We used a native SAD structure of DHFR:NADP$^+$:FOL, PDB: 7LVC, as the starting model (1), which was prepared by removing alternate conformations and protonating ionizable groups consistently with their local environments. We ran initial simulations in a 65 Å^3 waterbox, with 200 mM NaCl. We ran 20 independent simulations that included 10 ns of equilibration followed by 500 ns production runs, outputting frames every 250 ps. We analyzed the resulting trajectories using *MDTraj* (26).

MD Simulations of a DHFR Crystal. To simulate DHFR in its crystal context, we applied the $P2_12_12_1$ symmetry operations to the 7LVC starting model to build up the unit cell. We built a $3 \times 2 \times 1$ supercell by repeating the unit cell three times along the a axis and twice along the b axis. An important consideration for such simulations is the amount of water needed to maintain the crystallographic volume. We determined this using NPT "squeeze" runs, in which waters are added to the simulation box and strong distance restraints are slowly tapered off. More waters are then added or removed until the desired box volume is maintained within a user-determined tolerance (27). We automated this protocol in `mdtools` and used it to generate a $3 \times 2 \times 1$ DHFR supercell within 0.05% of the experimental volume. Additionally, we added chloride ions to the simulation box to neutralize the excess positive charge from the crystallographically observed manganese ions (1), which were included in these simulations. To equilibrate the system, we ran 50 ns of MD in an NPT ensemble. We then initialized production simulations in an NVT ensemble from the last frame of equilibration. We ran three independent production simulations for 500 ns, outputting frames every 100 ps.

Classification of Met20 loop substates in simulation. We quantified the population of the two Met20 loop substates using the Trp22-ϕ dihedral as a reporter. Since this dihedral exhibited two distinct states, we fit the data to a two-state Gaussian mixture model using all frames from each trajectory. We used the Gaussian mixture model implemented in *scikit-learn* for this analysis (28). To estimate the uncertainty in this classification, we classified the frames of each trajectory independently using the fit model and reported the mean and standard error across the trajectories. This analysis was repeated for the simulations of the solvated and lattice systems. For the solvated system, we used twenty independent trajectories to quantify the population of each substate. For the lattice system, we treated each protein molecules in the simulation independently, yielding 72 independent trajectories (24 protein molecules × 3 simulations).

Biased MD Simulations in Bulk Solvent. To validate that the results observed from X-ray diffraction experiments are recapitulated outside of the crystal context we ran MD simulations of the model of the DHFR Michaelis complex, using the same solvated simulation system as our unbiased trajectories. In order to bias the sampling of the MD simulations based on the hinge distance, we added a custom distance restraint between the C_α atoms of Asn23 and Pro53 using the following functional form:

$$U = \frac{1}{2}k(d - d_0)^2 \qquad [4]$$

where k was chosen to be 50.0 kcal/mol/Å^2, d is the distance between the C_α atoms of Asn23 and Pro53 under the minimum periodic image convention, and d_0 is the desired equilibrium distance for the active site cleft. We ran MD simulations with d_0 values of 18.8, 19.2, 19.6, 20.0, and 20.4 Å in order to bias the sampling across the range of crystallographically observed values. 100 independent simulations were equilibrated for 10 ns and then simulated for 100 ns for each value of d_0.

MD Simulations of the Reactive Ternary Complex in Bulk Solvent. Using the 7LVC starting model, we modeled NADPH and dihydrofolate (protonated and deprotonated) to represent the reactive ternary complex of DHFR. We prepared the simulation system in a 65 Å^3 waterbox with 200 mM of NaCl, and we ran 50 independent simulations with 10 ns of equilibration and then 100 ns production simulations.

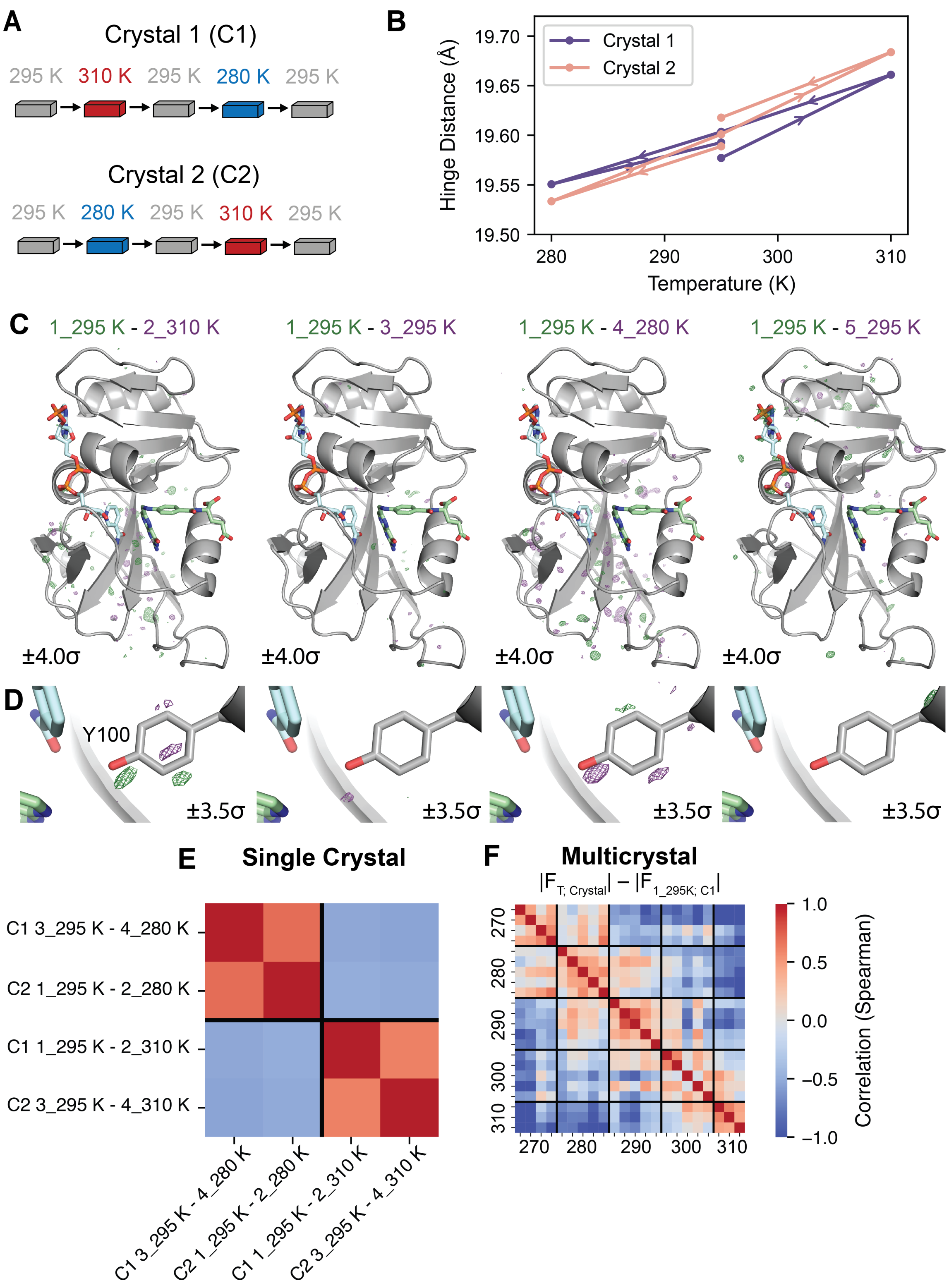

Fig. S1. Reversibility and reproducibility of multi-temperature diffraction experiments. (A) Schematic of single-crystal, multi-temperature diffraction experiments. (B) Plots of the refined hinge distance versus temperature for both single-crystal experiments demonstrate that the experiment is reversible. (C) Temperature-resolved difference maps between the first dataset from crystal 1 and the subsequent four datasets. More significant density peaks are observed for maps generated from datasets collected at different temperatures. (D) Zoom-in on Tyr100 in the difference maps emphasizes that observed features are temperature-dependent (carved within 2 Å of Tyr100). (E) Heatmap of the Spearman correlation coefficients between difference structure factor amplitudes computed from independent single-crystal experiments. Equivalent temperature changes yield strongly correlated difference amplitudes, while the opposite temperature changes produce strongly anti-correlated results. This demonstrates that the observed structural changes in the single-crystal, multi-temperature experiments are reproducible between independent experiments. (F) Heatmap of the Spearman correlation coefficients between difference structure factor amplitudes computed between different crystals. Although many temperature-resolved comparisons between crystals yield correlated results, there are several outlier crystals that could confound interpretation of the maps. This suggests that the single-crystal isomorphous difference maps yield more consistent results than maps computed from data derived from distinct crystals.

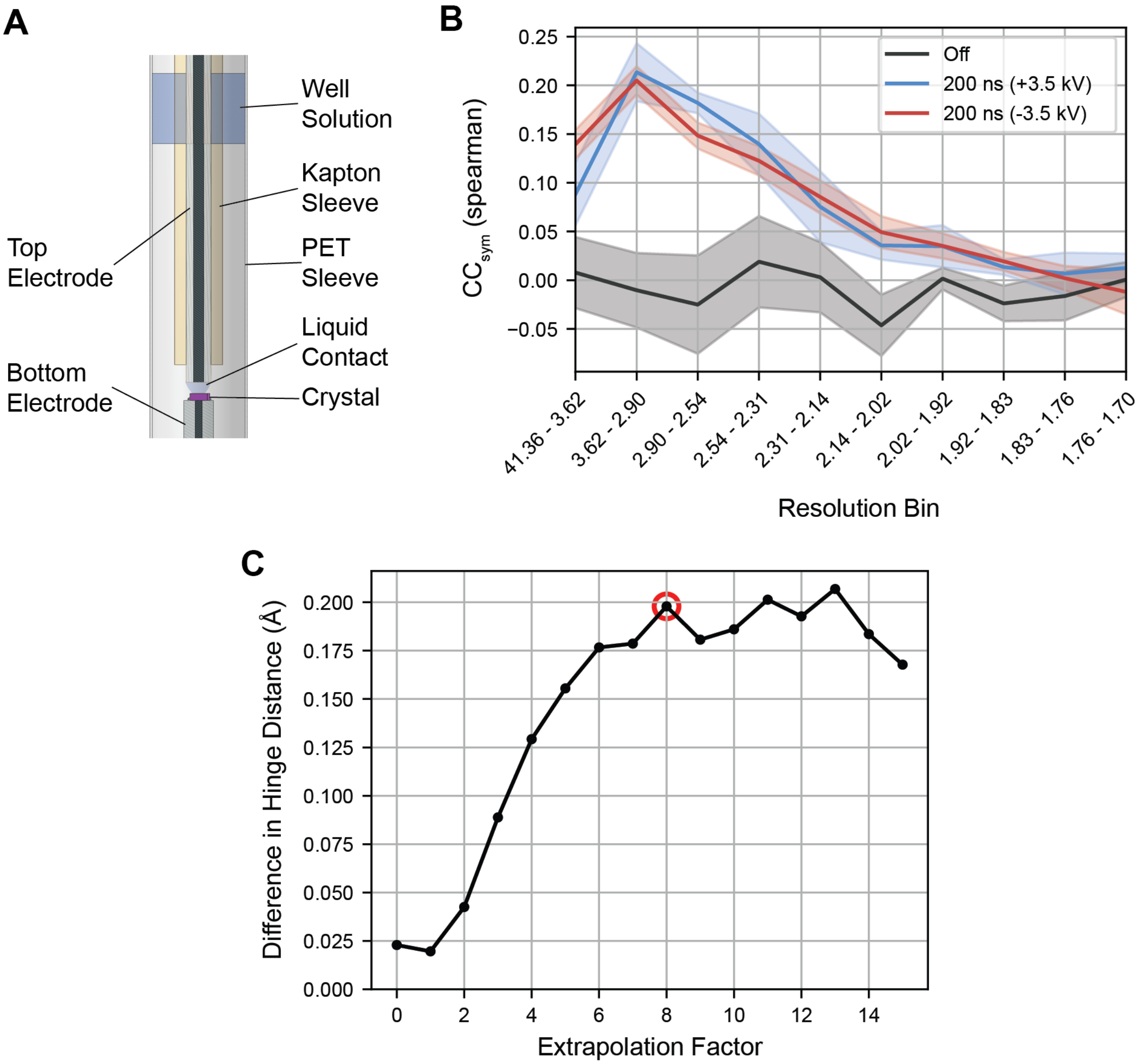

Fig. S2. Experimental apparatus and analysis for electric-field-stimulated X-ray diffraction of *ec*DHFR. (A) Diagram of the revised experimental apparatus for EF-X. Liquid contact is made within a band of well solution that is osmotically matched to the crystal, ensuring a high humidity environment for the duration of the experiment. (B) Plot of CC_{sym} versus resolution bin. CC_{sym} is an indicator of the reproducibility of observed symmetry breaking during an EF-X experiment. The 95% confidence interval from 5 random partitions of the diffraction images is shown. For the 'Off' dataset in which the symmetry operation is preserved, no significant correlation between half-datasets is expected because differences for symmetry-related observations should only reflect experimental error. The positive correlations for differences measured during the high-voltage pulses indicates significant electric-field-dependent symmetry breaking.(C) Plot of the refined difference in hinge distance between the two copies of DHFR in the $P2_1$ ASU as a function of extrapolation factor. With an extrapolation factor of zero, the data is equivalent to 'Off' structure factor amplitudes processed in the reduced-symmetry spacegroup. The difference in hinge distance increases linearly with extrapolation factor until a value of 8 and plateaus at a difference of approximately 0.2 Å. The extrapolation factor chosen for ESF refinement of the excited state is indicated with a red circle.

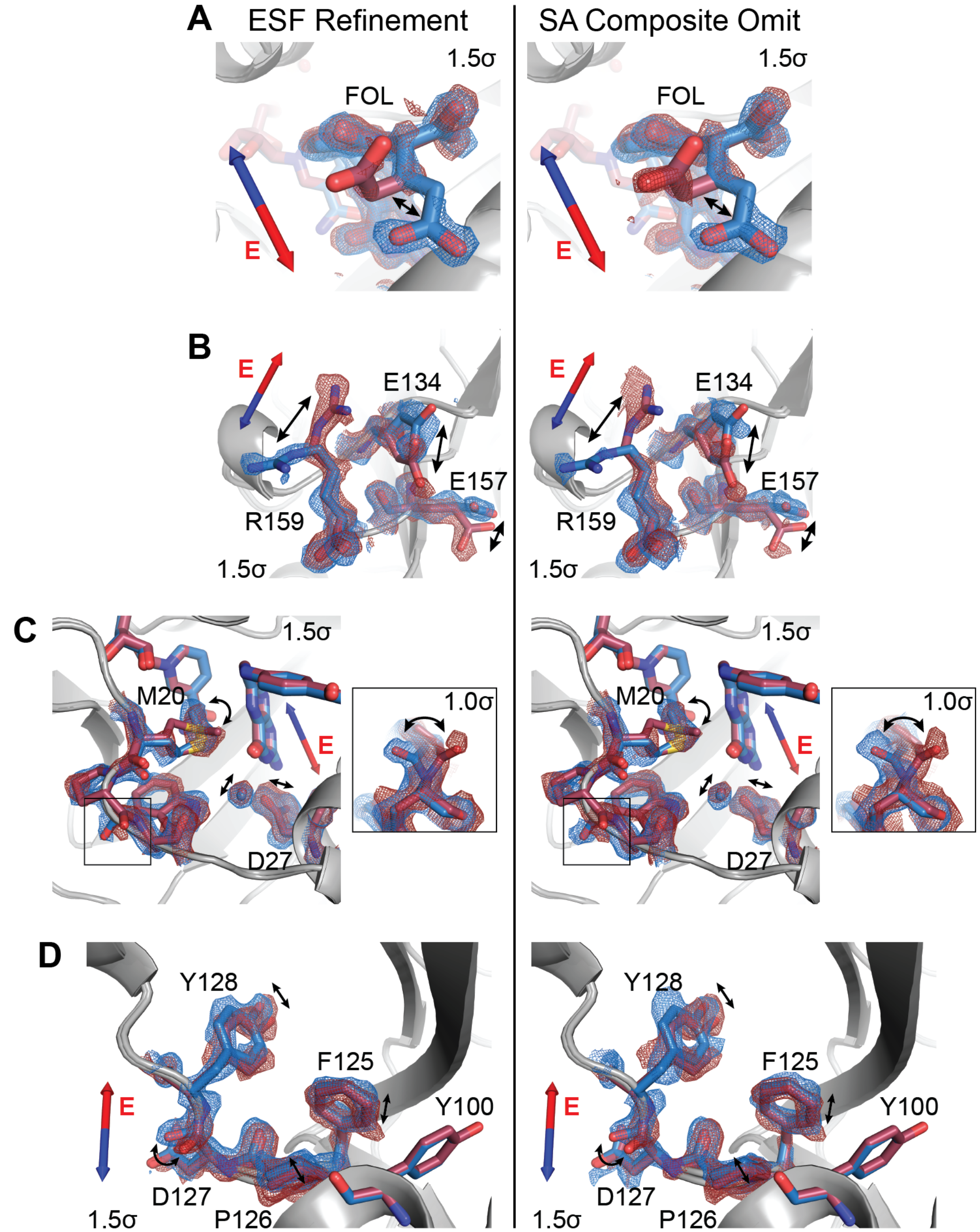

Fig. S3. Composite omit maps validate modeling of EF-X excited state. (A) to (D) Comparison of $2mF_o - DF_c$ maps from ESF refinement (left column) and corresponding simulated annealing (SA) composite omit maps (right column). Superposed models and maps from both protein molecules of the excited-state ASU highlight electric-field induced structural changes. Blue and red arrows depict electric field vector for the blue and red models, respectively, and maps are contoured at 1.5σ and carved within 1.5 Å of shown atoms. (A) Carboxylate sidechain of folate and (B) charged sidechains near the C-terminus demonstrate electric-field-dependent structural changes consistent with the formal charges of the residues. (C) Active site residues and Pro21 backbone carbonyl (inset; contoured at 1.0σ) differs between protein molecules. (D) Conformational changes among residues 125 to 128. The similarity between the electron density maps from ESF refinement and the SA composite omit maps indicates that the observed structural differences between the molecules of the excited-state ASU are not the result of modeling bias.

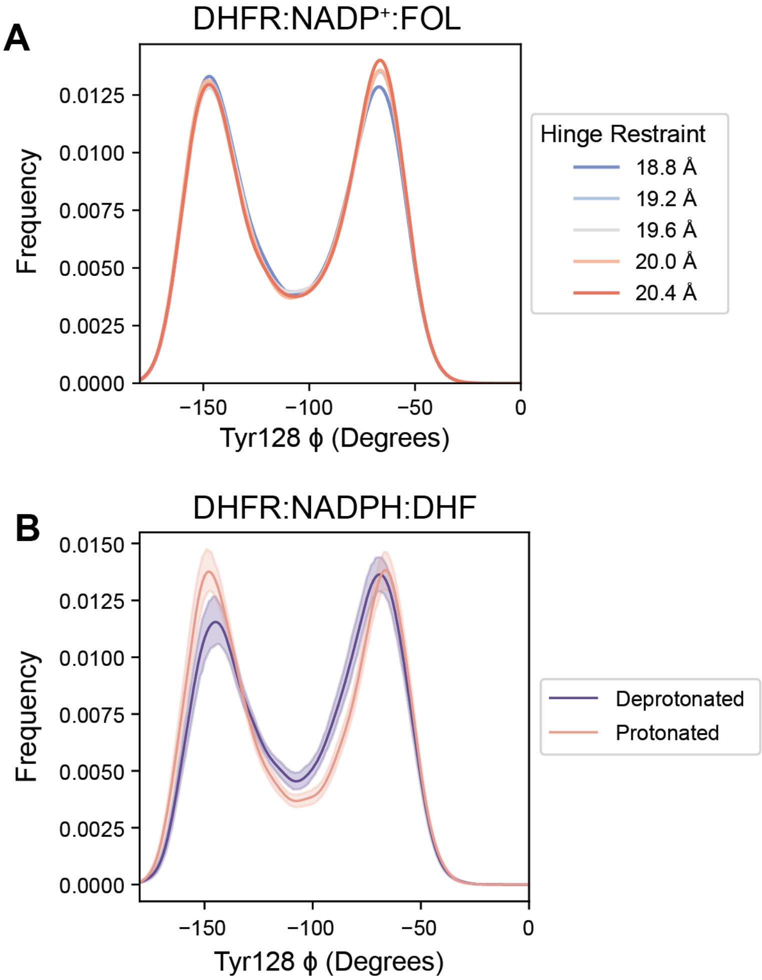

Fig. S4. Tyr128 backbone conformations in MD simulations. (A) Kernel density estimates of the Tyr128-ϕ dihedral from MD simulations at each imposed hinge distance restraint. The Tyr128-ϕ dihedral does not exhibit a monotonic relationship as a function of hinge distance. (B) Kernel density estimates of the Tyr128-ϕ dihedral from MD simulations of the reactive ternary complex (95% confidence interval is shown). The Tyr128-ϕ dihedral distribution is altered by substrate protonation.

Table S1. Summary statistics for DHFR:NADP$^+$:MFOL complex

PDB ID	8DAI
Temperature	285 K
Data Collection[1]	
Wavelength (Å)	0.9537
Spacegroup	$P2_12_12_1$
Cell dimensions (Å)	
a, b, c	34.25, 45.36, 98.85
Total observations	2,736,784
Unique observations	105,471
Resolution (Å)	49.42 - 1.14 (1.16 - 1.14)
Multiplicity	25.9 (14.4)
Completeness (%)	97.2 (73.0)
Mean I/σ_I	11.9 (0.4)
R_{pim}	0.028 (0.980)
$CC_{1/2}$	0.999 (0.326)
Refinement[2]	
R_{work} (%)	12.68
R_{free} (%)	16.00
R.M.S. Deviations	
Bonds (Å)	0.013
Angles (°)	1.357
Wilson B (Å^2)	15.57
Mean B factor (Å^2)	
Total	22.97
Macromolecules	21.07
Ligands	21.71
Water	39.71
Clashscore	2.23
Ramachandran	
Favored (%)	98.70
Allowed (%)	1.30
Outliers (%)	0.00

[1] Reported by *dials.scale* in *DIALS* (5)

[2] Reported by *PHENIX* (8)

Table S2. Summary statistics for datasets at 270 K

Crystal	1	2	3	4
PDB ID	5SSS	5SST	5SSU	5SSV
		Data Collection[1]		
Wavelength (Å)	0.8265	0.8265	0.8265	0.8265
Spacegroup	$P2_12_12_1$	$P2_12_12_1$	$P2_12_12_1$	$P2_12_12_1$
Cell dimensions (Å)				
a	34.11	34.08	34.10	34.12
b	45.34	45.29	45.18	45.26
c	99.11	99.00	99.09	99.06
Total observations	2,999,634	3,330,004	3,101,071	3,366,693
Unique observations	107,967	128,870	109,637	125,784
Resolution (Å)	49.56 - 1.14 (1.16 - 1.14)	33.41 - 1.07 (1.09 - 1.07)	32.24 - 1.12 (1.14 - 1.12)	45.26 - 1.08 (1.10 - 1.08)
Multiplicity	27.8 (28.1)	25.8 (27.6)	28.3 (29.5)	26.8 (27.7)
Completeness (%)	99.8 (99.9)	98.7 (96.6)	96.3 (93.6)	98.8 (96.5)
Mean I/σ_I	13.7 (0.7)	22.5 (1.5)	18.6 (0.5)	19.7 (0.4)
R_{pim}	0.077 (2.382)	0.101 (2.200)	0.134 (2.876)	0.077 (3.610)
$CC_{1/2}$	0.999 (0.400)	0.999 (0.551)	0.999 (0.415)	0.999 (0.309)
		Refinement[2]		
R_{work} (%)	14.70	13.00	13.93	13.98
R_{free} (%)	16.74	14.82	16.89	17.38
R.M.S. Deviations				
Bonds (Å)	0.010	0.007	0.008	0.012
Angles (°)	1.085	1.018	1.027	1.237
Wilson B (Å^2)	16.04	15.50	15.85	15.12
Mean B factor (Å^2)				
Total	21.71	21.28	22.90	21.95
Macromolecules	20.11	19.64	21.16	20.29
Ligands	19.14	18.73	20.27	19.27
Water	37.28	36.80	39.62	38.19
Clashscore	1.57	1.27	0.94	1.57
Ramachandran				
Favored (%)	99.35	99.35	99.35	99.35
Allowed (%)	0.65	0.65	0.65	0.65
Outliers (%)	0.00	0.00	0.00	0.00

[1] Reported by *dials.scale* in *DIALS* (5)

[2] Reported by *PHENIX* (8)

Table S3. Summary statistics for datasets at 280 K

Crystal	1	2	3	4	5
PDB ID	7FPL	7FPM	7FPN	7FPO	7FPP
			Data Collection[1]		
Wavelength (Å)	0.8265	0.8265	0.8265	0.8265	0.8265
Spacegroup	$P2_12_12_1$	$P2_12_12_1$	$P2_12_12_1$	$P2_12_12_1$	$P2_12_12_1$
Cell dimensions (Å)					
a	34.12	34.16	34.14	34.18	34.20
b	45.50	45.51	45.44	45.55	45.47
c	99.05	99.08	99.04	99.08	99.09
Total observations	2,800,998	3,839,113	3,322,423	3484869	3,946,244
Unique observations	98,434	142,620	141,821	135,454	134,271
Resolution (Å)	32.26 - 1.17 (1.19 - 1.17)	45.51 - 1.04 (1.06 - 1.04)	45.44 - 1.04 (1.06 - 1.04)	45.55 - 1.06 (1.08 - 1.06)	32.33 - 1.03 (1.05 - 1.03)
Multiplicity	28.4 (28.4)	26.9 (20.5)	23.4 (18.5)	25.7 (25.4)	29.4 (28.1)
Completeness (%)	97.8 (96.7)	99.5 (96.4)	99.2 (93.1)	99.9 (98.4)	90.6 (59.8)
Mean I/σ_I	18.0 (0.7)	19.6 (0.4)	19.8 (0.4)	18.4 (0.5)	28.7 (0.5)
R_{pim}	0.054 (1.586)	0.061 (2.520)	0.212 (4.479)	0.106 (2.364)	0.018 (1.327)
$CC_{1/2}$	0.999 (0.343)	0.999 (0.309)	0.998 (0.388)	0.999 (0.336)	0.999 (0.324)
			Refinement[2]		
R_{work} (%)	14.39	12.91	13.55	14.74	12.51
R_{free} (%)	16.53	15.31	15.84	17.07	14.90
R.M.S. Deviations					
Bonds (Å)	0.007	0.010	0.008	0.009	0.010
Angles ($^\circ$)	0.970	1.156	1.031	1.133	1.154
Wilson B (Å^2)	16.14	14.76	15.35	15.41	14.82
Mean B factor (Å^2)					
Total	21.99	21.06	21.84	22.07	21.36
Macromolecules	20.38	19.34	20.12	20.39	19.66
Ligands	19.42	18.54	19.03	19.30	18.60
Water	37.56	37.65	38.53	38.45	37.89
Clashscore	1.89	1.26	1.57	1.89	1.57
Ramachandran					
Favored (%)	99.35	99.35	99.35	99.35	99.35
Allowed (%)	0.65	0.65	0.65	0.65	0.65
Outliers (%)	0.00	0.00	0.00	0.00	0.00

[1] Reported by *dials.scale* in *DIALS* (5)

[2] Reported by *PHENIX* (8)

Table S4. Summary statistics for datasets at 290 K

Crystal	1	2	3	4	5
PDB ID	7FPR	7FPS	7FPT	7FPU	7FPV
			Data Collection[1]		
Wavelength (Å)	0.8265	0.8265	0.8265	0.8265	0.8265
Spacegroup	$P2_12_12_1$	$P2_12_12_1$	$P2_12_12_1$	$P2_12_12_1$	$P2_12_12_1$
Cell dimensions (Å)					
a	34.18	34.19	34.19	34.18	34.20
b	45.49	45.56	45.59	45.60	45.56
c	99.10	99.05	99.05	99.07	99.04
Total observations	3,627,079	2,149,046	3,640,008	3,834,528	3,765,323
Unique observations	125,984	80,476	123,429	132,517	142,372
Resolution (Å)	32.31 - 1.07 (1.09 - 1.07)	49.53 - 1.26 (1.28 - 1.26)	32.32 - 1.07 (1.09 - 1.07)	32.31 - 1.05 (1.07 - 1.05)	41.39 - 1.04 (1.06 - 1.04)
Multiplicity	28.8 (29.4)	26.7 (23.3)	29.5 (30.2)	28.9 (27.8)	26.4 (20.7)
Completeness (%)	95.6 (92.8)	99.8 (98.4)	93.5 (90.4)	94.8 (80.5)	99.2 (95.4)
Mean I/σ_I	23.7 (0.6)	18.6 (1.1)	25.8 (0.8)	24.5 (0.6)	27.8 (0.5)
R_{pim}	0.111 (2.284)	0.105 (1.704)	0.028 (1.401)	0.027 (1.713)	0.031 (1.101)
$CC_{1/2}$	0.999 (0.312)	0.999 (0.357)	0.999 (0.555)	0.999 (0.349)	0.999 (0.364)
			Refinement[2]		
R_{work} (%)	12.37	13.17	11.84	12.25	12.60
R_{free} (%)	14.62	16.65	14.22	14.72	14.50
R.M.S. Deviations					
Bonds (Å)	0.008	0.009	0.009	0.009	0.007
Angles (°)	1.035	1.083	1.144	1.124	1.025
Wilson B (Å^2)	14.98	15.94	15.00	15.29	14.11
Mean B factor (Å^2)					
Total	23.05	22.82	21.68	21.81	21.80
Macromolecules	21.04	20.95	19.93	20.10	19.84
Ligands	19.85	20.08	18.66	18.81	18.35
Water	42.52	40.85	38.81	38.55	41.08
Clashscore	1.26	2.20	1.57	1.57	1.89
Ramachandran					
Favored (%)	99.35	99.35	99.35	99.35	99.35
Allowed (%)	0.65	0.65	0.65	0.65	0.65
Outliers (%)	0.00	0.00	0.00	0.00	0.00

[1] Reported by *dials.scale* in *DIALS* (5)

[2] Reported by *PHENIX* (8)

Table S5. Summary statistics for datasets at 300 K

Crystal PDB ID	1 7FPX	2 7FPY	3 7FPZ	4 7FQ0	5 7FQ1
			Data Collection[1]		
Wavelength (Å)	0.8265	0.8265	0.8265	0.8265	0.8265
Spacegroup	$P2_12_12_1$	$P2_12_12_1$	$P2_12_12_1$	$P2_12_12_1$	$P2_12_12_1$
Cell dimensions (Å)					
a	34.14	34.14	34.09	34.23	34.24
b	45.41	45.44	45.19	45.53	45.38
c	99.04	99.00	98.89	99.14	99.23
Total observations	3,350,065	2,995,768	1,824,827	2,913,593	2,666,016
Unique observations	134,806	114,032	69,305	104,829	95,421
Resolution (Å)	49.52 - 1.06	99.00 - 1.12	49.44 - 1.32	45.53 - 1.15	32.36 - 1.18
	(1.08 - 1.06)	(1.14 - 1.12)	(1.34 - 1.32)	(1.17 - 1.15)	(1.20 - 1.18)
Multiplicity	24.8 (24.7)	26.3 (26.9)	26.3 (26.8)	27.8 (28.3)	27.9 (28.4)
Completeness (%)	99.9 (98.7)	99.7 (99.7)	99.9 (99.9)	98.4 (97.7)	97.1 (96.3)
Mean I/σ_I	20.6 (0.5)	18.7 (0.6)	15.7 (0.7)	25.0 (0.5)	22.0 (0.4)
R_{pim}	0.162 (5.383)	0.128 (3.646)	0.409 (1.023)	0.038 (1.358)	0.059 (1.140)
$CC_{1/2}$	0.999 (0.346)	0.999 (0.364)	0.997 (0.443)	0.999 (0.334)	0.999 (0.312)
			Refinement[2]		
R_{work} (%)	12.90	14.11	14.34	13.28	14.19
R_{free} (%)	15.41	17.01	18.19	16.20	17.67
R.M.S. Deviations					
Bonds (Å)	0.014	0.011	0.007	0.006	0.006
Angles (°)	1.357	1.127	0.977	0.935	0.875
Wilson B (Å^2)	15.54	15.64	16.72	15.23	15.89
Mean B factor (Å^2)					
Total	22.97	22.97	23.59	24.08	23.89
Macromolecules	21.12	21.14	21.68	21.91	21.99
Ligands	19.50	19.62	20.84	20.53	20.69
Water	41.23	40.98	42.02	45.20	42.40
Clashscore	2.52	1.89	1.89	1.57	1.26
Ramachandran					
Favored (%)	99.35	99.35	99.35	99.35	99.35
Allowed (%)	0.65	0.65	0.65	0.65	0.65
Outliers (%)	0.00	0.00	0.00	0.00	0.00

[1] Reported by *dials.scale* in *DIALS* (5)

[2] Reported by *PHENIX* (8)

Table S6. Summary statistics for datasets at 310 K

Crystal	1	2	3
PDB ID	7FQ3	7FQ4	7FQ5
Data Collection[1]			
Wavelength (Å)	0.8265	0.8265	0.8265
Spacegroup	$P2_12_12_1$	$P2_12_12_1$	$P2_12_12_1$
Cell dimensions (Å)			
a	34.18	34.15	34.19
b	45.49	45.23	45.30
c	99.33	99.22	99.25
Total observations	1,969,232	1,829,107	1,788,359
Unique observations	73,267	67,810	65,420
Resolution (Å)	41.36 - 1.30 (1.32 - 1.30)	33.42 - 1.33 (1.36 - 1.33)	99.25 - 1.35 (1.37 - 1.35)
Multiplicity	26.9 (27.1)	27.3 (28.6)	27.3 (28.9)
Completeness (%)	99.4 (92.4)	99.1 (97.9)	99.5 (89.5)
Mean I/σ_I	15.4 (0.4)	24.5 (0.6)	21.3 (0.5)
R_{pim}	0.310 (1.596)	0.080 (0.848)	0.108 (1.048)
$CC_{1/2}$	0.997 (0.360)	0.999 (0.301)	0.999 (0.328)
Refinement[2]			
R_{work} (%)	15.24	14.61	14.96
R_{free} (%)	18.66	18.57	18.96
R.M.S. Deviations			
Bonds (Å)	0.006	0.008	0.009
Angles (°)	1.001	1.037	1.007
Wilson B (Å^2)	17.48	15.77	17.55
Mean B factor (Å^2)			
Total	23.71	24.37	25.03
Macromolecules	21.58	22.22	22.77
Ligands	20.69	21.76	21.86
Water	44.24	44.80	46.82
Clashscore	1.89	2.20	3.15
Ramachandran			
Favored (%)	99.35	99.35	99.35
Allowed (%)	0.65	0.65	0.65
Outliers (%)	0.00	0.00	0.00

[1] Reported by *dials.scale* in *DIALS* (5)

[2] Reported by *PHENIX* (8)

Table S7. Summary statistics for multi-crystal, multi-temperature datasets

Temperature	270 K	280 K	290 K	300 K	310 K
PDB ID	5SSW	7FPQ	7FPW	7FQ2	7FQ6
Number of Crystals	4	5	5	5	3
Data Collection[1]					
Wavelength (Å)	0.8265	0.8265	0.8265	0.8265	0.8265
Spacegroup	$P2_12_12_1$	$P2_12_12_1$	$P2_12_12_1$	$P2_12_12_1$	$P2_12_12_1$
Cell dimensions (Å)					
a	34.10	34.16	34.19	34.14	34.18
b	45.28	45.50	45.56	45.41	45.30
c	99.08	99.08	99.05	99.04	99.25
Total observations	14,601,731	19,116,204	19,028,898	17,134,249	6,176,809
Unique observations	133,686	147,105	142,798	131,221	74,931
Resolution (Å)	49.54 - 1.06	45.50 - 1.03	49.53 - 1.04	99.04 - 1.07	99.25 - 1.29
	(1.08 - 1.06)	(1.05 - 1.03)	(1.06 - 1.04)	(1.09 - 1.07)	(1.31 - 1.29)
Multiplicity	109.1 (107.6)	129.9 (87.0)	133.2 (101.9)	130.5 (128.3)	82.2 (84.7)
Completeness (%)	99.4 (96.5)	99.8 (96.3)	99.5 (96.0)	100.0 (100.0)	99.8 (94.0)
Mean I/σ_I	36.9 (1.4)	45.5 (0.7)	44.0 (0.8)	38.5 (0.8)	31.6 (0.6)
R_{pim}	0.050 (2.423)	0.045 (3.530)	0.052 (15.696)	0.170 (1.657)	0.098 (0.839)
$CC_{1/2}$	1.000 (0.446)	1.000 (0.429)	1.000 (0.398)	1.000 (0.557)	1.000 (0.326)
Refinement[2]					
R_{work} (%)	12.34	11.83	11.55	12.13	13.96
R_{free} (%)	14.39	13.84	13.52	14.38	17.89
R.M.S. Deviations					
Bonds (Å)	0.009	0.008	0.009	0.010	0.012
Angles (°)	1.137	1.072	1.167	1.146	1.161
Wilson B (Å^2)	15.47	15.24	14.64	15.13	18.97
Mean B factor (Å^2)					
Total	21.22	21.27	21.71	23.43	25.21
Macromolecules	19.62	19.53	19.85	21.38	23.07
Ligands	18.63	18.61	18.14	19.53	22.40
Water	36.78	37.65	40.14	43.78	45.87
Clashscore	1.89	1.57	1.57	2.20	2.20
Ramachandran					
Favored (%)	99.35	99.35	99.35	99.35	99.35
Allowed (%)	0.65	0.65	0.65	0.65	0.65
Outliers (%)	0.00	0.00	0.00	0.00	0.00

[1] Reported by *dials.scale* in *DIALS* (5)

[2] Reported by *PHENIX* (8)

Table S8. Summary statistics for single-crystal, multi-temperature datasets (crystal 1)

Temperature	295 K	310 K	295 K	280 K	295 K
Pass on Crystal	1	2	3	4	5
PDB ID	7FQ7	7FQ8	7FQ9	7FQA	7FQB
			Data Collection[1]		
Wavelength (Å)	0.8265	0.8265	0.8265	0.8265	0.8265
Spacegroup	$P2_12_12_1$	$P2_12_12_1$	$P2_12_12_1$	$P2_12_12_1$	$P2_12_12_1$
Cell dimensions (Å)					
a	34.26	34.29	34.27	34.20	34.22
b	45.59	45.65	45.63	45.46	45.47
c	98.96	99.03	98.97	98.99	99.02
Total observations	3,400,772	2,601,689	3,315,426	3,572,742	3,053,872
Unique observations	117,634	89,462	115,024	123,443	105,250
Resolution (Å)	32.37 - 1.10 (1.12 - 1.10)	41.46 - 1.21 (1.23 - 1.21)	41.44 - 1.11 (1.13 - 1.11)	32.32 - 1.08 (1.10 - 1.08)	32.34 - 1.14 (1.16 - 1.14)
Multiplicity	28.9 (28.8)	29.1 (29.5)	28.8 (28.6)	28.9 (29.0)	29.0 (28.0)
Completeness (%)	96.7 (95.6)	97.6 (96.6)	97.1 (96.4)	96.5 (94.5)	96.6 (96.2)
Mean I/σ_I	12.8 (0.3)	14.1 (0.4)	12.6 (0.3)	12.7 (0.3)	13.5 (0.4)
R_{pim}	0.027 (1.213)	0.037 (1.105)	0.029 (1.257)	0.025 (1.426)	0.028 (1.245)
$CC_{1/2}$	0.999 (0.324)	0.999 (0.380)	0.999 (0.354)	0.999 (0.311)	0.999 (0.332)
			Refinement[2]		
R_{work} (%)	12.80	12.64	13.13	13.11	13.36
R_{free} (%)	15.89	16.40	15.94	15.89	16.48
R.M.S. Deviations					
Bonds (Å)	0.008	0.011	0.007	0.005	0.006
Angles (°)	1.054	1.192	1.008	0.884	0.953
Wilson B (Å^2)	17.06	16.74	17.13	17.26	16.81
Mean B factor (Å^2)					
Total	22.18	23.86	23.34	21.75	22.30
Macromolecules	20.38	21.68	21.54	20.09	20.46
Ligands	18.80	19.14	19.88	18.77	18.97
Water	39.94	45.87	41.17	38.11	40.38
Clashscore	1.26	2.20	1.26	1.26	1.89
Ramachandran					
Favored (%)	99.35	99.35	99.35	99.35	99.35
Allowed (%)	0.65	0.65	0.65	0.65	0.65
Outliers (%)	0.00	0.00	0.00	0.00	0.00

[1] Reported by *dials.scale* in *DIALS* (5)

[2] Reported by *PHENIX* (8)

Table S9. Summary statistics for single-crystal, multi-temperature datasets (crystal 2)

Temperature	295 K	280 K	295 K	310 K	295 K
Pass on Crystal	1	2	3	4	5
PDB ID	7FQC	7FQD	7FQE	7FQF	7FQG
			Data Collection[1]		
Wavelength (Å)	0.9795	0.9795	0.9795	0.9795	0.9795
Spacegroup	$P2_12_12_1$	$P2_12_12_1$	$P2_12_12_1$	$P2_12_12_1$	$P2_12_12_1$
Cell dimensions (Å)					
a	34.26	34.20	34.25	34.30	34.28
b	45.63	45.52	45.60	45.71	45.68
c	99.03	99.06	99.09	99.12	99.04
Total observations	2,722,807	2,756,746	2,721,740	2,438,928	2,674,944
Unique observations	97,218	99,044	97,041	86,426	95,020
Resolution (Å)	49.52 - 1.18 (1.20 - 1.18)	49.53 - 1.17 (1.19 - 1.17)	49.55 - 1.18 (1.20 - 1.18)	49.56 - 1.23 (1.25 - 1.23)	49.52 - 1.19 (1.21 - 1.19)
Multiplicity	28.0 (23.7)	27.8 (21.2)	28.0 (23.8)	28.2 (28.4)	28.1 (26.5)
Completeness (%)	98.5 (94.9)	98.2 (91.2)	98.4 (94.4)	98.9 (98.2)	98.6 (95.5)
Mean I/σ_I	13.0 (0.4)	12.8 (0.4)	12.6 (0.4)	12.3 (0.3)	12.1 (0.4)
R_{pim}	0.033 (1.029)	0.031 (1.107)	0.033 (1.127)	0.044 (1.404)	0.038 (1.220)
$CC_{1/2}$	0.999 (0.359)	0.999 (0.308)	0.999 (0.308)	0.999 (0.321)	0.999 (0.333)
			Refinement[2]		
R_{work} (%)	12.74	14.09	12.88	13.06	13.13
R_{free} (%)	16.00	16.17	16.38	16.91	16.41
R.M.S. Deviations					
Bonds (Å)	0.008	0.008	0.009	0.013	0.005
Angles (°)	1.028	1.030	1.114	1.238	0.905
Wilson B (Å^2)	17.21	17.63	17.19	17.08	16.96
Mean B factor (Å^2)					
Total	22.47	21.53	22.56	25.06	22.56
Macromolecules	20.65	19.92	20.71	22.89	20.73
Ligands	19.14	18.95	19.18	20.60	19.09
Water	40.35	37.10	40.75	46.94	40.71
Clashscore	2.20	1.89	2.20	2.20	1.57
Ramachandran					
Favored (%)	99.35	99.35	99.35	99.35	99.35
Allowed (%)	0.65	0.65	0.65	0.65	0.65
Outliers (%)	0.00	0.00	0.00	0.00	0.00

[1] Reported by *dials.scale* in *DIALS* (5)

[2] Reported by *PHENIX* (8)

Table S10. Data reduction statistics for DHFR EF-X from Laue diffraction

Dataset	Off	Off (reduced sym.)	200 ns (+3.5 kV)	200 ns (-3.5 kV)
No. of Images	363	363	363	363
Spacegroup	$P2_12_12_1$	$P2_1$	$P2_1$	$P2_1$
Cell dim. (Å)				
a	34.29	34.29	34.29	34.29
b	45.53	45.53	45.53	45.53
c	99.00	99.00	99.00	99.00
Total obs.	723,372	723,372	710,019	709,472
Unique obs.	17,637	33,671	33,671	33,669
Resolution (Å)	41.36 - 1.70 (1.76 - 1.70)	41.36 - 1.70 (1.76 - 1.70)	41.36 - 1.70 (1.76 - 1.70)	49.50 - 1.70 (1.76 - 1.70)
Multiplicity	35.53 (27.40)	18.63 (14.16)	18.35 (13.73)	18.34 (13.68)
Completeness (%)	99.5 (99.4)	99.4 (99.5)	99.4 (99.5)	99.4 (99.5)
Mean F/σ_F[1]	39.38 (19.51)	28.54 (14.00)	28.85 (13.86)	28.85 (13.83)
$CC_{1/2}$[1]	0.991 (0.957)	0.987 (0.927)	0.989 (0.929)	0.988 (0.929)

[1] Statistics were computed based on output from *careless* (15)

Table S11. Refinement statistics for DHFR EF-X[1]

Dataset	Off	On
PDB ID	8G4Z	8G50
Spacegroup	$P2_12_12_1$	$P2_1$
Extrapolation factor	N/A	8
Resolution (Å)	1.70	1.70
Unique observations	17,636	33,646
Completeness	99.43	99.26
R_{work} (%)	14.71	30.37
R_{free} (%)	19.53	34.98
R.M.S. Deviations		
Bonds (Å)	0.009	0.011
Angles (°)	1.15	1.09
Mean B factor (Å^2)		
Total	8.53	5.54
Macromolecules	7.52	5.16
Ligands	7.74	4.81
Water	20.08	9.97
Clashscore	2.01	3.05
Ramachandran		
Favored (%)	99.35	99.35
Allowed (%)	0.65	0.65
Outliers (%)	0.00	0.00

[1] Reported by *PHENIX* (8)

References

1. JB Greisman, et al., Native sad phasing at room temperature. *Acta Crystallogr. Sect. D* **78**, 986–996 (2022).
2. GJ Correy, et al., The mechanisms of catalysis and ligand binding for the SARS-CoV-2 NSP3 macrodomain from neutron and x-ray diffraction at room temperature. *Sci. Adv.* **8**, eabo5083 (2022).
3. OB Zeldin, M Gerstel, EF Garman, *RADDOSE-3D*: time- and space-resolved modelling of dose in macromolecular crystallography. *J. Appl. Crystallogr.* **46**, 1225–1230 (2013).
4. CS Bury, JC Brooks-Bartlett, SP Walsh, EF Garman, Estimate your dose: Raddose-3d. *Protein Sci.* **27**, 217–228 (2018).
5. G Winter, et al., *DIALS*: implementation and evaluation of a new integration package. *Acta Crystallogr. Sect. D* **74**, 85–97 (2018).
6. J Beilsten-Edmands, et al., Scaling diffraction data in the *DIALS* software package: algorithms and new approaches for multi-crystal scaling. *Acta Crystallogr. Sect. D* **76**, 385–399 (2020).
7. PA Karplus, K Diederichs, Linking crystallographic model and data quality. *Science* **336**, 1030–1033 (2012).
8. PV Afonine, et al., Towards automated crystallographic structure refinement with *phenix.refine*. *Acta Crystallogr. Sect. D* **68**, 352–367 (2012).
9. P Virtanen, et al., SciPy 1.0: fundamental algorithms for scientific computing in Python. *Nat. Methods* **17**, 261–272 (2020).
10. CR Harris, et al., Array programming with NumPy. *Nature* **585**, 357–362 (2020).
11. T Ursby, D Bourgeois, Improved estimation of structure-factor difference amplitudes from poorly accurate data. *Acta Crystallogr. Sect. A* **53**, 564–575 (1997).
12. M Schmidt, et al., Ligand migration pathway and protein dynamics in myoglobin: A time-resolved crystallographic study on L29W MbCO. *Proc. Natl. Acad. Sci.* **102**, 11704–11709 (2005).
13. JB Greisman, KM Dalton, DR Hekstra, *reciprocalspaceship*: a Python library for crystallographic data analysis. *J. Appl. Crystallogr.* **54**, 1521–1529 (2021).
14. DR Hekstra, et al., Electric-field-stimulated protein mechanics. *Nature* **540**, 400–405 (2016).
15. KM Dalton, JB Greisman, DR Hekstra, A unifying Bayesian framework for merging X-ray diffraction data. *Nat. Commun.* **13**, 7764 (2022).
16. UK Genick, et al., Structure of a protein photocycle intermediate by millisecond time-resolved crystallography. *Science* **275**, 1471–1475 (1997).
17. MD Winn, et al., Overview of the *CCP*4 suite and current developments. *Acta Crystallogr. Sect. D* **67**, 235–242 (2011).
18. A Hodel, SH Kim, AT Brünger, Model bias in macromolecular crystal structures. *Acta Crystallogr. Sect. A* **48**, 851–858 (1992).
19. TC Terwilliger, et al., Iterative-build OMIT maps: map improvement by iterative model building and refinement without model bias. *Acta Crystallogr. Sect. D* **64**, 515–524 (2008).
20. P Eastman, et al., OpenMM 7: Rapid development of high performance algorithms for molecular dynamics. *PLOS Comput. Biol.* **13**, 1–17 (2017).
21. JA Maier, et al., ff14SB: Improving the accuracy of protein side chain and backbone parameters from ff99SB. *J. Chem. Theory Comput.* **11**, 3696–3713 (2015).
22. WL Jorgensen, J Chandrasekhar, JD Madura, RW Impey, ML Klein, Comparison of simple potential functions for simulating liquid water. *The J. Chem. Phys.* **79**, 926–935 (1983).
23. J Wang, RM Wolf, JW Caldwell, PA Kollman, DA Case, Development and testing of a general amber force field. *J. Comput. Chem.* **25**, 1157–1174 (2004).
24. N Holmberg, U Ryde, L Bülow, Redesign of the coenzyme specificity in L-lactate dehydrogenase from *Bacillus stearothermophilus* using site-directed mutagenesis and media engineering. *Protein Eng. Des. Sel.* **12**, 851–856 (1999).
25. KL Meagher, LT Redman, HA Carlson, Development of polyphosphate parameters for use with the amber force field. *J. Comput. Chem.* **24**, 1016–1025 (2003).
26. RT McGibbon, et al., Mdtraj: A modern open library for the analysis of molecular dynamics trajectories. *Biophys. J.* **109**, 1528 – 1532 (2015).
27. DS Cerutti, PL Freddolino, REJ Duke, DA Case, Simulations of a protein crystal with a high resolution x-ray structure: Evaluation of force fields and water models. *J. Phys. Chem. B* **114**, 12811–12824 (2010).
28. F Pedregosa, et al., Scikit-learn: Machine learning in Python. *J. Mach. Learn. Res.* **12**, 2825–2830 (2011).